Pulse envelope effects in nonlinear Breit-Wheeler pair creation

S. Tang[1] and B. King[2,*]

[1]*College of Physics and Optoelectronic Engineering,*
Ocean University of China, Qingdao, Shandong 266100, China
[2]*Centre for Mathematical Sciences, University of Plymouth, Plymouth PL4 8AA, United Kingdom*

The effect of the pulse envelope on electron-positron pair creation in a circularly polarized laser pulse is investigated. Interference on the length scale of the pulse envelope, and smoothness of the pulse edges are found to influence the pair spectrum. A toy model of a flat-top pulse is used to identify pulse envelope effects inaccessible to local approaches. Broadening of channel openings and a widening of the energy and transverse momentum distribution of the pair are found to receive contributions that are below the local harmonic threshold. By comparing pair yields in a flat-top, sine-squared and Gaussian pulse, a link between pulse shape and photon-polarized Breit-Wheeler pair creation is found. In the transverse momentum distribution, a signal of pulse envelope interference is found in an azimuthal asymmetry, which appears in intense fields and persists in long pulses.

I. INTRODUCTION

The conversion of two photons to an electron-positron pair was calculated by Breit and Wheeler in the 1930s [1]. The decay of a *single* photon into an electron-positron pair in a classical electromagnetic field, is often referred to as the "nonlinear Breit-Wheeler" process. "Nonlinear" refers to the dependency on the charge-field coupling, which generally can depend on high powers of the field intensity. One of the challenges in calculating this process in a classical background is that the amplitude can depend strongly on how the background varies in space and time. This can include interference from the process happening at different points in the background, and gradient effects from the rising and falling edge of the pulse. These effects can mean that if the process is approximated by splitting the background into infinitesimally short intervals, using the probability for the process to occur in a constant (and crossed) field in each interval and then integrating over all the intervals the background was split into, the result can differ substantially from the correct one. For high field intensities this procedure can, however, in general provide a good approximation, which is often referred to as the "locally constant field approximation" (LCFA) [2–8], and is the central approximation by which quantum electrodynamical (QED) effects in intense classical backgrounds, such as the nonlinear Breit-Wheeler process [9–31], are included into numerical simulation frameworks [32–41].

In this paper, we will consider the situation where the background field has two time scales. This is a relevant situation for, e.g. experiments involving a laser

pulse, which has the fast time scale of the carrier frequency, and the slow time scale of the pulse envelope. For a strongly focused laser pulse, there may be other relevant time scales, but we will model the laser pulse here as a plane wave, which should be a good approximation for a weakly focused pulse. We will consider laser intensities that are routinely attained with weak focusing in the lab.

The LCFA depends on the single parameter, χ, the "quantum nonlinearity parameter," which has no explicit reference to any length scale of the field. Therefore, the LCFA can be thought to include interference effects on the sub-wavelength scale. (The length scale over which interference effects play a role, is sometimes referred to as the "formation length" [2].) The advantage is that the LCFA can be employed when the form of the classical background is not known *a priori*. An alternative approximation, which is useful when the form of the background is close to a plane wave and is known not to change substantially in interactions with e.g., a probe beam, is the locally monochromatic approximation (LMA) [42]. The LMA treats the fast time scale of the carrier frequency exactly and neglects derivatives of the pulse envelope. It depends on two parameters: the classical nonlinearity parameter ξ, which is proportional to λ, the wavelength of the background, and the (quantum) energy parameter, η, proportional to $1/\lambda$. Therefore the LMA can be thought to include interference effects on the length scale of the wavelength (the "fast" time scale). In the limit of large ξ and large outgoing particle energy, the LMA depends only on the product $\chi = \xi\eta$, and tends to the LCFA, with all explicit dependency on the background having disappeared. The explicit definitions of ξ and η will be given in Sec. II.

Motivation for the current study comes from planned upcoming experiments, such as E320 at SLAC and LUXE [43] at DESY, which will use a conventionally accelerated electron beam of $O(10 \text{ GeV})$, to measure the nonlinear Breit-Wheeler process in the "all-order" region where the charge-field coupling, described by the classical nonlinearity parameter, ξ, is $\sim O(1)$. The interaction point of the LUXE experiment is modeled using the simulation code Ptarmigan [44], which implements the LMA for the nonlinear Compton [45] and nonlinear Breit-Wheeler [46] processes. (A similar approximation framework [47] was implemented to model the E144 experiment [48,49], and was also used in CAIN [50] and IPStrong [51].) To understand what is missed in local approaches is therefore worthy of investigation.

The current paper will find two main effects that are missed by local or "instantaneous" approaches. One effect is due to interference on the length scale of the pulse envelope (i.e., the "slow" time scale). Therefore, in addition to ξ and η, the number of laser cycles, N, which is proportional to the pulse length, will be used to specify the input parameters. These effects persist in magnitude (although they may move to lower energies) as the pulse length is increased. Another effect is due to derivatives of the pulse envelope, which are missed by local approaches that only include the leading-order derivative (i.e., the gradient) of the background. We will find that these effects can be increased (decreased) in amplitude by making the pulse envelope edges steeper (shallower), as quantified by the bandwidth of the Fourier transform.

One may think that interference effects over long spacetime scales are less important for pair creation than e.g., for Compton scattering because pair creation is typically strongly suppressed for lower field strengths, and so only a small region around the laser pulse peak field strength would contribute. (This is an explanation that follows when $\xi \gg 1$; see e.g., Ref. [52].) However, for lower field strengths, it is exactly this strong suppression, which makes the process sensitive to bandwidth effects around the carrier frequency of the pulse.

The effect the pulse envelope can have on nonlinear Breit-Wheeler pair creation has been investigated already in several works by direct numerical evaluation of the QED expressions, or by using a "slowly varying" envelope approach. Line-broadening and sub-threshold enhancement have been identified in triple differential spectra [12], and an enhancement in energy spectra in the multiphoton region in circularly [15] and linearly polarized [16] laser pulses has been linked to finite bandwidth effects. Short, circularly polarized pulses lead to an asymmetry in the azimuthal spectrum of produced pairs [53], which is sensitive to the pulse's carrier envelope phase [54,55]. When double pulses are used, various pulse shape effects can arise and be controlled [23,56–58], and multiple pulses can lead to coherent enhancement [59]. There also exist some

analytical solutions for nonlinear Breit-Wheeler pair creation in special ultra-short plane-wave pulses [27,28]. Apart from Breit-Wheeler pair creation, the pulse envelope's shape can also be crucial in determining pair creation via the dynamically assisted Sauter-Schwinger effect [60–64].

To investigate pulse envelope effects, we will use a combination of direct numerical evaluation of QED calculations for plane-wave pulses as well as an analytical "toy model" of a circularly polarized "flat-top" monochromatic pulse. This toy model has the advantage that any deviation from the locally monochromatic spectrum can only be caused by pulse-envelope interference, as it is only at the beginning and end of the pulse where there is a variation in the field strength. Therefore these deviations are *beyond* a locally monochromatic (and therefore beyond a locally constant) approximation.

Three different pulse envelopes will be referred to in this paper, which are depicted in Fig. 1, centred on the origin for comparison purposes. The flat-top envelope is described by $g(\varphi) = 1$ for $0 < \varphi < \Phi$ with $g(\varphi) = 0$ otherwise. The sine-squared pulse is an example of a finite smooth pulse with the envelope $g(\varphi) = \sin^2(\pi\varphi/\Phi)$ for $0 < \varphi < \Phi$ with $g(\varphi) = 0$ otherwise. The Gaussian pulse envelope is an example of an infinitely extended, smooth pulse, defined as $g(\varphi) = \exp[-2.3(2\varphi/\Phi)^2]$. The choice of the Gaussian exponential factor is such that the amplitude is 10% of its peak value at the edge of the sine-squared pulse. Since we are studying nonlinear Breit-Wheeler pair creation, which is strongly dependent on the intensity parameter, the value of 10% was chosen so that two pulses were approximately equal around the peak of the pulse (see Fig. 1).

The paper is organized as follows. In Sec. II the flat-top potential toy model is introduced and the effect on the total yield of pairs, the light-front momentum spectrum, and the angular spectrum is illustrated. In Sec. III, a leading-order perturbative analysis is given, corresponding to linear Breit-Wheeler pair creation, and a link between pulse duration and photon polarization is shown. In Sec. IV,
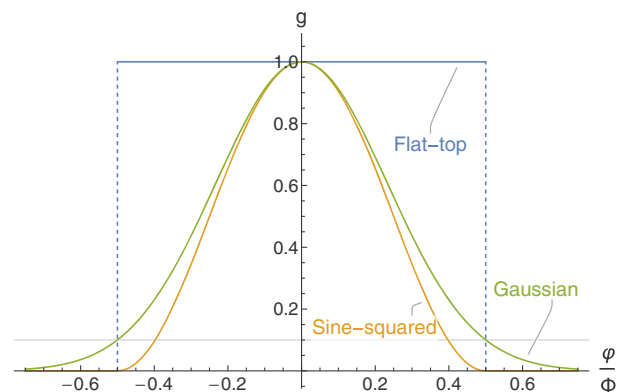

FIG. 1. Three different normalized pulse shapes, g, used in the current paper, centered at the origin.

the direct numerical evaluation of the QED expressions for a flat-top, sine-squared and Gaussian pulse are presented and azimuthal asymmetry in the angular spectrum of pairs is identified as a signal of pulse interference. We use natural units $\hbar = c = 1$ throughout and the fine-structure constant is $\alpha = e^2 \approx 1/137$.

II. TOY MODEL: FLAT-TOP POTENTIAL

Consider a circularly polarized potential of the form

$$a = m\xi(0, \cos\varphi, \sin\varphi, 0), \qquad 0 < \varphi < \Phi$$

(otherwise $a = 0$), where $a = |e|A$, ξ is the normalized potential, $\varphi = \varkappa \cdot x$ is the background phase, and $\varkappa = \varkappa^0(1, 0, 0, 1)$, where $\varkappa^0$ is the laser carrier frequency. The normalized potential is also the classical nonlinearity parameter ξ and can be defined in a Lorentz- and gauge-invariant way [65] as $\xi = (|e|/m)[\langle k \cdot F \cdot k \rangle_\tau / (\varkappa \cdot k)^2]^{1/2}$, where F is the Faraday tensor, k is the momentum of the probe particle and $\langle \cdot \rangle_\tau$ is a proper time average.

The pulse phase length is $\Phi = 2N\pi$, where N is the number of laser cycles. The energy parameter, $\eta = (k + \varkappa)^2/2m^2 = \varkappa \cdot k/m^2$ is a linear quantum parameter and characterizes the center-of-mass energy of the collision. In Ref. [66], nonlinear Compton scattering was studied in this background, while here we calculate nonlinear Breit-Wheeler pair creation.

Here, we give the main expressions and definitions for the probability of nonlinear Breit-Wheeler pair creation, P (more details about the method can be found in Ref. [67]):

$$\mathsf{P} = \frac{\alpha}{(2\pi\eta)^2} \int \frac{dt d^2 \mathbf{r}^\perp}{t(1-t)} \int d\varphi d\varphi' e^{i \int_{\varphi'}^{\varphi} d\phi \frac{k \cdot \pi_q(\phi)}{\eta m^2 (1-t)}}$$
$$\times [\Delta\Delta' + h(t)(a^2\Delta' - 2a \cdot a' + a'^2\Delta)/(2m^2)], \quad (1)$$

where $t = \varkappa \cdot q/\varkappa \cdot k$, q^μ is the asymptotic momentum of the positron after leaving the potential and k^μ is the photon momentum, $\mathbf{r}^\perp = \mathbf{q}^\perp/m - t\mathbf{k}^\perp/m$, $a = a(\varphi)$ and $a' = a(\varphi')$, with $h(t) = (1 - 2t + 2t^2)/[2t(1-t)]$. The instantaneous momentum of the positron in the field, π_q is

$$\pi_q = q - a + \frac{q \cdot a}{k \cdot q}\varkappa - \frac{a^2}{2k \cdot q}\varkappa, \quad (2)$$

and

$$\Delta = 1 - \frac{k \cdot \pi_q}{k \cdot q} = \frac{2m\mathbf{r}^\perp \cdot \mathbf{a} - \mathbf{a}^2}{m^2[1 + (\mathbf{r}^\perp)^2]}, \quad (3)$$

where Δ' is analogous to Δ but with $\mathbf{a}(\varphi)$ replaced with $\mathbf{a}(\varphi')$.

To specialize Eq. (1) to the flat-top potential, we employ the Jacobi-Anger expansion and integrate over the azimuthal transverse coordinate. This yields a total probability

that can be written as a sum over harmonics, n: $\mathsf{P} = \alpha/\eta \sum_{n=\lceil n_* \rceil}^{\infty} \mathcal{I}_n$ where $\lceil n_* \rceil$ denotes the lowest integer greater than or equal to n_*, and here for the flat-top potential, $n_* = -\infty$. Then $\mathcal{I}_n$ is given by[1]

$$\mathcal{I}_n = \frac{\Phi}{\eta} \int \frac{dt dr^2}{t(1-t)} \delta_\Phi \left[\frac{r^2 - r_\infty^2}{2\eta t(1-t)} \right] \{ w^2 J_n^2(z) - \xi^2 h(t)$$
$$\times [2w J_n^2(z) - J_{n+1}^2(z) - J_{n-1}^2(z)]/2 \}, \quad (4)$$

with $r = |\mathbf{r}^\perp|$, where $z = \xi r/\eta t(1-t)$ and we have defined the regularized delta function

$$\delta_\Phi(x) = \frac{\Phi}{2\pi}\text{sinc}^2\left(\frac{\Phi x}{2}\right), \quad (5)$$

($\text{sinc} x = \sin x/x$) and the finite-duration factor w is

$$w = \frac{1 + r_\infty^2}{1 + r^2}; \qquad r_\infty^2 = 2n\eta t(1-t) - (1 + \xi^2).$$

The function $\delta_\Phi(x)$ tends to the Dirac delta function $\delta(x)$ in the infinite pulse-length limit of $\Phi \to \infty$. In this limit, the finite-duration factor $w \to 1$ and Eq. (4) tends to the locally monochromatic (and infinite monochromatic [10]) result. As remarked in Ref. [66], the function δ_Φ can be written in terms of harmonics as

$$\delta_\Phi(n - \tilde{n}_*), \qquad \text{where:} \; \tilde{n}_* = \frac{1 + \xi^2 + r^2}{2\eta t(1-t)}. \quad (6)$$

Our analysis of the result, Eq. (4), will focus on the description in terms of harmonics.

A. Harmonic channel opening

In the locally monochromatic approach, we can acquire a "threshold" harmonic $n_* \to \tilde{n}_*$ from Eq. (6), by finding the minimum of $\tilde{n}_*$, which occurs when $r = 0$ and $t = 1/2$, i.e., $n_* = 2(1 + \xi^2)/\eta$. When the locally monochromatic approach is applied to a pulse, $a(\varphi)$, different parts of the pulse can have different threshold harmonics, and therefore access different harmonic "channels" to pair creation. In the local approach, we can see that having a nonconstant pulse envelope implies that some channels become accessible, that would otherwise not be, if just the average pulse intensity was assumed. However, in the flat-top model, because $a(\varphi)$ is constant everywhere (apart from the edges of the pulse), this local effect *cannot* access any channel opening behavior.

When we take into account the finite pulse effect and evaluate Eq. (4), we see several differences to the local approach.

---

[1]The result in Eq. (4) has been numerically verified by direct evaluation of Eq. (1) in a flat-top background.

(i) Each harmonic is "broadened." In the local approach, as $\delta_\Phi(\cdot) \to \delta(\cdot)$ once the momentum of the pair is given, the harmonic order is fixed to be $n = \tilde{n}_*$. However, since the pulse is finite in phase, it has a finite bandwidth in the light-front momentum it can supply to the pair.

(ii) There is no longer a threshold harmonic. The central peak of δ_Φ has a width such that the main contribution is for a harmonic n within the range approximately bounded by $\tilde{n}_* \pm \pi/\Phi$. The $n = 0$ channel is opened and short pulses allow for the contribution from negative harmonics.

(iii) The wave vector of the background $\varkappa$, and therefore also the energy parameter η are no longer constant. A Fourier transform of the background of a pulse reveals a width of momenta around the "central" carrier envelope frequency.

The situation can be demonstrated by the use of a Mandelstam plot. Using momentum conservation in a monochromatic wave

$$k + n\varkappa = \bar{p} + \bar{q}, \qquad (7)$$

where $\bar{p} = p - \varkappa(a^2/2\varkappa \cdot p)$ (and likewise for $\bar{q}$) is the quasimomentum of the electron (positron), we can define the Mandelstam variables $\bar{s} = (k + n\varkappa)^2/m^2 = 2n\eta$, $\bar{t} = (\bar{q} - n\varkappa)^2/m^2 = 1 + \xi^2 - 2tn\eta$ and $\bar{u} = (\bar{p} - n\varkappa)^2/m^2 = 1 + \xi^2 - 2(1 - t)n\eta$. We see that, for fixed background momentum $\varkappa$ and positive harmonic n, the variables $\bar{t}$ and $\bar{u}$ cannot exceed $1 + \xi^2$. This defines a physically accessible region, highlighted in Fig. 2. For the monochromatic case, ξ is constant and using the threshold condition $n_* \geq 2(1 + \xi^2)/\eta$, we see that $\bar{s} \geq 4(1 + \xi^2)$. This region is highlighted in Fig. 2, where for each harmonic, there is a curve of values in the $(\bar{t}, \bar{u})$ plane given by varying the parameter t between 0 and 1. The locally monochromatic

region would in general allow access to "subthreshold" harmonics because $0 \leq \xi(\varphi) \leq \xi$. The corresponding region is also highlighted in the figure. In contrast, in a finite pulse, Eq. (7) no longer holds absolutely, due to the pulse edges spoiling the periodic symmetry along the pulse propagation direction. This nonconservation is quantified by the regularized delta function (6). In principle the bandwidth can be wide enough that all harmonics, including $n = 0$ and negative n, are kinematically accessible. (In the figure, the finite pulse region is suggested as stretching into a region around the one accessible by a local approach). This is particularly relevant for a flat-top pulse, the Fourier transform of which is a sinc-squared function, which, having an inverse-square dependency on frequency, has a particularly wide bandwidth (this point will be developed later).

We calculate the effect of these new harmonic channels on the total pair yield in Fig. 3. Their contribution can be seen most clearly in two places: (i) in the low-energy region $\eta \ll 1$; (ii) for parameter values close to a harmonic transition.

Close to a harmonic transition, the "broadness" of the harmonic can be clearly seen in Fig. 3. Even though the number of laser cycles N (related to pulse duration via $\Phi = 2\pi N$) is large enough to be in the long-pulse regime where one would expect the locally monochromatic approximation to work well, we see that the contribution from the new harmonic channels remains approximately independent of energy, with rising "edge" structures close to each harmonic.

Also in the multiphoton regime $\xi \ll 1$, whereas a local approach gives a pair yield that is power-law suppressed as $\sim \xi^{2n_*}$ [68], which for small enough ξ, leads to a strong suppression, and the flat-top pulse result does not suffer such a suppression. The reason for this is that the finite pulse result has access to the *linear Breit-Wheeler* process, due to the broad bandwidth of the flat-top envelope, which
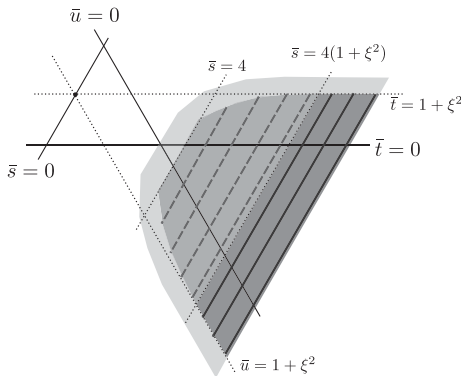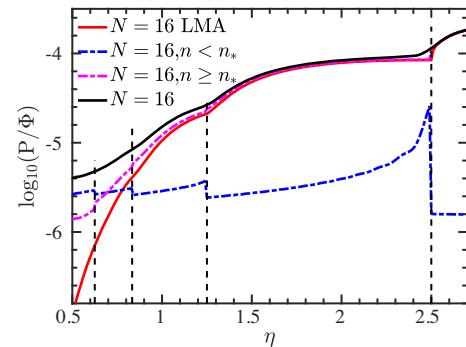

FIG. 2. Mandelstam plot for the Breit-Wheeler process. Kinematically accessible regions are highlighted: monochromatic case (darkest shaded region, solid harmonics lines); locally monochromatic (mid-darkest shaded region, long-dashed harmonic lines); finite pulse (bandwidth suggested by lightest shaded region).

FIG. 3. The opening of harmonic channels as the collision energy parameter η is increased, for $\xi = 0.5$ and $N = 16$ laser cycles. Vertical dashed lines correspond to the position of the lowest harmonic in the locally monochromatic approach: $n_* = 1$, 2, 3, 4 from right to left. The lowest harmonic accessible in the local approach is given as $\lceil n_* \rceil$, where $n_* = 2(1 + \xi^2)/\eta$.

is kinematically forbidden in the local approach. (This fact has already been investigated in several works in the context of universality [62,69], but here we link it explicitly to a harmonic analysis.) (The linear Breit-Wheeler case is studied in more detail later on.) Therefore this "enhancement" at small η or small ξ is to do with the smoothness of the pulse shape. We note that this enhancement is contributed to by harmonics *above* and *below* threshold.

B. Light-front momentum spectrum

The finite bandwidth of the background also affects the shape of light-front momentum spectra. In the local approach, most pairs are produced with the electron and positron having similar light-front momenta (i.e., the spectrum has a peak around $t = 1/2$.). The probability for one of the pair to take much more of the probe photon's light-front momentum than the other, is heavily suppressed (i.e., the spectrum is suppressed at large/small t). However, in the flat-top case, shorter pulses can greatly enhance the *relative* proportion of pairs whose constituents can carry very different light-front momenta. This is illustrated in Fig. 4(a): the shorter the pulse, the flatter the spectrum, but even for long pulses, the enhancement is clearly visible for higher values of asymmetry as $t \to 1$. In particular, the *absolute* enhancement is *independent* of the pulse duration, suggesting it originates in the higher derivatives at the rising and trailing edges of the pulse. (We calculated the light-front momentum spectrum in the smoother pulse shapes of a sine-squared and Gaussian background, and the asymmetry effect diminishes substantially, showing it to be a consequence of the wide bandwidth of a flat-top pulse.) Which harmonics are contributing to this enhancement, is demonstrated in Fig. 4(b). We see that, indeed the maximum contribution agrees with the locally monochromatic case, but that there is an important region just below the monochromatic threshold, stretching to $n = -1$, which is entirely missed by local approaches. As the pulse is made shorter, the relative contribution increases from these
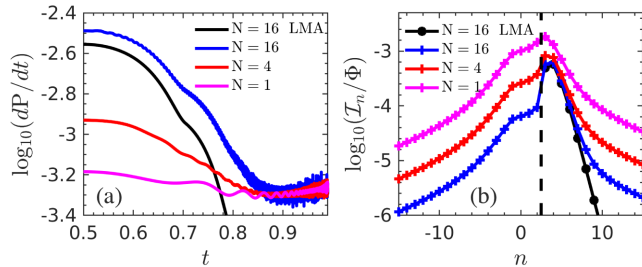
"below threshold" harmonics and the light-front momentum spectrum flattens.

C. Transverse momentum distribution

As a further demonstration of the role of the extra harmonic channels, in Fig. 5, we plot the combined light-front and transverse momentum dependency of produced positron yield for the case $\xi = 0.5, \eta = 1, N = 4$. There are three main differences brought about by the pulse envelope. i) Since the suppression of larger light-front momentum fractions is softened in the finite pulse cases, there are more harmonics visible in the large-/small-t part of the spectrum in Fig. 5(a) compared to the plot of harmonics only accessible in the locally monochromatic approach in Fig. 5(b). The contribution from harmonics inaccessible to a local approach, is shown in Fig. 5(c). ii) There appear subharmonics between the main harmonic lines in Fig. 5(b), which correspond to the subpeaks in the regularized delta function in Eq. (4). The subthreshold harmonics lines in Fig. 5(c) can further brighten these subharmonics in the whole yield in Fig. 5(a) but also lead to a splitting of the main harmonics at large/small t. iii) A peak occurs at low transverse momentum (the $r \to 0$ region) due to the opening of the $|n| \leq 1$ harmonic channels in the flat-top pulse. This link can be understood by considering the regularized delta function in r^2 in Eq. (4). In the locally monochromatic approach, the radial position squared of each harmonic is given by

$$r_\infty^2(\varphi) = 2n\eta t(1 - t) - [1 + \xi^2(\varphi)], \qquad (8)$$

and $r^2(\varphi) = r_\infty^2(\varphi)$. The minimum perpendicular momentum is then at $r^2 \approx \lceil n_* \rceil \eta/2 - 1$. However, in the flat-top pulse, considering the additional width of each harmonic supplied by the pulse envelope, we see $r^2(\varphi)$ is approximately in the interval given by $r_\infty^2(\varphi) \pm \eta t(1 - t)/N$. So we should expect that there is a signal in the transverse
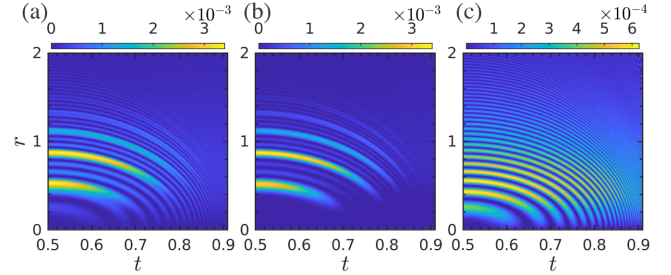

FIG. 4.   For $\xi = 0.5$ and $\eta = 1$. Left: the light-front momentum fraction spectrum of the produced positrons. Because of the symmetry $d\mathsf{P}(t)/dt = d\mathsf{P}(1 - t)/dt$ in (1), we only plot the spectrum with $t \geq 0.5$. Right: the contribution of each harmonic, n, where the vertical dashed line is the lowest harmonic accessible in the locally monochromatic case.

FIG. 5.   Double differential in transverse momentum parameter r and light-front momentum fraction t of positron yield $d^2\mathsf{P}/dtdr$. (a) All the harmonic channels open in the flat-top pulse; (b) only the harmonics accessible in a local monochromatic approach, $n \geq n_*$; (c) harmonics inaccessible to the local approach, $n < n_*$. The results are for $\xi = 0.5, \eta = 1, N = 4$.

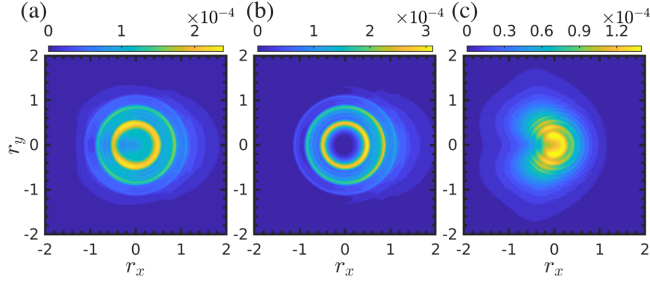FIG. 6. Double differential in the transverse momentum parameters of the positron yield $d^2\mathsf{P}/dr_x dr_y$. (a) All the harmonic channels open in the flat-top pulse; (b) only the harmonics accessible in a local monochromatic approach, $n \geq n_*$; (c) harmonics inaccessible to the local approach, $n < n_*$. All the parameters are the same as in Fig. 5.

momentum distribution (TMD) due to the pulse envelope, at smaller transverse momenta than predicted by the local approach. Because this is to do with the width of each harmonic and contains the length scale $2N\lambda$ [substituting $n \to 1$ and $\eta \to \eta \pm \eta/2N$ in Eq. (8) leads to the additional width supplied by the pulse envelope], it can be related to interference on the length scale of the pulse envelope. (A similar behavior of the appearance of a linear peak appearing at small r was noted for the Compton scattering in a flat-top pulse [66].) (It was also recently observed that the enhancement of harmonics at lower values of r can be understood by considering angular-momentum conservation in the absorption of laser photons producing the pair [70].)

Finally, another role of the finite pulse duration shown in Fig. 6 is to induce an azimuthal asymmetry in the positron yield distribution [55]. As shown in the figure, this asymmetry appears not only in the distribution of the positron yield from the harmonics accessible in the local approach, but also in the distribution from the extra harmonic channels opened by the finite pulse effect [Figs. 6(b) and (c) respectively]. This asymmetry affects the *entire* TMD and is enhanced in *short* pulses. Therefore, it is associated with the shape of the pulse and higher-derivative effects. In contrast, in Sec. IV, we will demonstrate an asymmetry at the *center* of the TMD, to do with pulse-envelope interference.

III. LINEAR BREIT-WHEELER

It was shown in the previous section that finite pulse envelope effects are particularly strong in the multiphoton regime at low background intensity. The reason for this is simply that the yield, when calculated with a local approach, is so strongly suppressed in this regime, that the effect due to the pulse envelope, which is otherwise small, becomes dominant. In this section, we analyze the contribution to the yield to leading order in ξ^2—also known as *linear* Breit-Wheeler pair creation. The dominance of

pulse effects in the low-intensity (and strongly suppressed) region has already been highlighted in the literature (see e.g., Refs. [15,16]), and so here, we concentrate on the role of the negative harmonics, and in doing so, will reveal a connection between photon polarization channels and pulse duration.

We can acquire the leading-order perturbative probability, P_ℓ either by perturbatively expanding the integrand in Eq. (1) and keeping only $O(\xi^2)$ terms, or by calculating the linear Breit-Wheeler process from first principles in a plane-wave background. In order to aid interpretation, we define a momentum contributed by the background field, $\nu\varkappa$, through the relation

$$\nu\varkappa + k = p + q,$$

where $\nu = \bar{s}/2\eta$, which is the center-of-mass energy squared in units of $2\eta m^2$. This is useful because ν is the ratio of light-front momentum supplied by the background over the light-front momentum supplied by the carrier wave (i.e., the monochromatic limit), and so quantifies how wide the pulse's bandwidth must be to facilitate the process. The probability for the linear Breit Wheeler process is then:

$$\mathsf{P}_\ell = \frac{\alpha}{\pi\eta} \int_0^1 dt \int_{\nu_*}^\infty d\nu \frac{|\tilde{\mathbf{a}}(\nu)|^2}{m^2} \left[\frac{1}{2} h(t) + \frac{\nu/\nu_* - 1}{\nu^2/\nu_*^2} \right] \quad (9)$$

where $\nu_*(t) = 1/[2\eta t(1 - t)]$ is the threshold parameter required to create a pair with zero transverse momentum $(r^2 = 0)$ and $\tilde{\mathbf{a}}(\nu) = \int d\varphi \mathbf{a}(\varphi) e^{i\varphi\nu}$.

The result in Eq. (9) clearly demonstrates the threshold requirement $\nu > \nu_*$ to create a pair. We see that $\nu_* \propto 1/\eta$, i.e., the lower the photon energy, the higher the momentum required from the background to create a pair. For a plane-wave pulse then, the contribution depends on how the Fourier spectrum decays as the frequency is varied away from the carrier frequency. For the flat-top potential,

$$\frac{|\tilde{\mathbf{a}}(\nu)|^2}{m^2} = \frac{\xi^2 \Phi^2}{2} \left[\text{sinc}^2 \frac{\Phi(\nu + 1)}{2} + \text{sinc}^2 \frac{\Phi(\nu - 1)}{2} \right] \quad (10)$$

i.e., the spectrum has peaks at $\nu = \pm 1$, but each with a width that decays as $\sim 1/\Phi^2$. Here we see the reason why the pulse-envelope effect is dominant in the multiphoton regime. For the monochromatic case, $\mathsf{P} \sim \xi^{2n_*}$, with $n_* = 2(1 + \xi^2)/\eta$, and so when $\eta \ll 1$, which is typical for modern-day laser-particle experiments, there is a strong decay in the pair yield as ξ is reduced since $n_* \gg 1$. Contrast this with the linear Breit-Wheeler contribution from the envelope, which only decays as ξ^2, but is suppressed by a constant factor that depends on the envelope's bandwidth. Eventually, for sufficiently small ξ, the linear Breit-Wheeler effect, which originates from the pulse envelope, will dominate the total signal for pair creation.
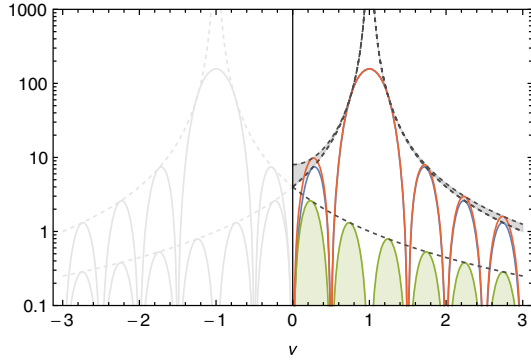
FIG. 7. Fourier spectrum of potential for a two-cycle flat-top pulse ($\Phi = 4\pi$). Only the absorption of positive frequencies can kinematically contribute to pair creation, but in a short pulse, these can arise from the wide bandwidth of the *negative* frequency part of the spectrum. Envelopes are plotted with dashed lines and the contribution from the $n = -1$ harmonic, and the net difference, are both highlighted.

The role of negative harmonics can also be clearly seen in the perturbative result. In Fig. 7, we plot the Fourier transform of the flat-top pulse spectrum, Eq. (10). The spectrum decays away from the positive [negative] frequency peak, approximately as $\sim(\nu - 1)^{-2}$ $[(\nu + 1)^{-2}]$. The positive (negative) frequency peaks correspond to the $n = 1$ ($n = -1$) harmonics of the background. For a sufficiently short pulse, or equivalently, broad bandwidth, there is a significant contribution from the negative-frequency peak, that can extend to the positive-frequency range. This is another visualization of the effect discussed in the Mandelstam plot Fig. 2: negative harmonics can contribute in kinematically accessible regions. We emphasize that here in the perturbative case, $n = -1$ corresponds to the negative-frequency component of the pulse. One should contrast this with the nonperturbative case discussed in the previous section and for larger values of ξ, where $n = -1$ corresponds to one *net* "photon" being emitted back to the background.

A. Polarization signal

The contribution of the negative harmonic to linear Breit-Wheeler pair creation suggests a further effect due to the pulse envelope, on the relative contribution to each photon-polarisation channel. This can be seen by considering a head-on collision between the photon and a plane-wave laser pulse. The potential for a circularly polarized pulse can be written in the form

$$a(\varphi) = g(\varphi)[\Lambda_- e^{i\varphi} + \Lambda_+ e^{-i\varphi}], \qquad (11)$$

where $g(\varphi)$ is the envelope and $\Lambda_\pm = (\Lambda_1 \pm i\Lambda_2)/2$ are light-front helicity states of the probe photon,

$$\Lambda_{1,2} = \varepsilon_{1,2} - \frac{k \cdot \varepsilon_{1,2}}{k \cdot \varkappa}\varkappa, \qquad (12)$$

for a head-on collision with $k = k^0(1, 0, 0, -1)$, and in the coordinates used so far in this paper, $\varepsilon_1 = (0, 1, 0, 0)$, $\varepsilon_2 = (0, 0, 1, 0)$. From Eq. (11), we see that different helicity states are associated with the positive- and negative-frequency parts of the background. Whereas a circularly polarized probe photon will couple to just the Λ_+ or Λ_- state alone, a linearly polarized photon, being a superposition of circularly polarized states, will be able to couple the Λ_+ and Λ_- states together at the level of the probability [which contains a $(a \cdot \epsilon)^2$ term, for photon polarization ϵ]. Therefore, for a linearly polarized photon, a part of the probability will be proportional to the overlap of the positive- and negative-frequency parts of the spectrum. In this way, a connection between pulse duration and probe photon polarization is made.

For a linearly polarized photon propagating in the circularly polarized background, the linear Breit-Wheeler probability is

$$P_\ell = \frac{\alpha}{\pi\eta} \int_0^1 dt \int_{\nu_*}^\infty d\nu \left[\frac{|\tilde{a}(\nu)|^2}{m^2} \left(\frac{1}{2} h(t) + \frac{\nu/\nu_* - 1}{\nu^2/\nu_*^2} \right) \right.$$
$$\left. + \Gamma \frac{|\tilde{a}_y(\nu)|^2 - |\tilde{a}_x(\nu)|^2}{2m^2\nu^2/\nu_*^2} \right], \qquad (13)$$

where $\tilde{a}_x$ ($\tilde{a}_y$) is the x (y) component of the Fourier-transformed vector potential, $\Gamma = 1$ if the photon is in polarization state Λ_1, and $\Gamma = -1$ if the photon is in polarization state Λ_2. Defining $\tilde{g}(\nu) = \int d\varphi\, g(\varphi) \exp[i\varphi\nu]$, we see that the unpolarized part of the probability is proportional to

$$|\tilde{a}(\nu)|^2 \propto |\tilde{g}(\nu + 1)|^2 + |\tilde{g}(\nu - 1)|^2.$$

However, the polarized part is proportional to the overlap of the positive- and negative-frequency components:

$$|\tilde{a}_y(\nu)|^2 - |\tilde{a}_x(\nu)|^2 \propto \tilde{g}(\nu + 1)\tilde{g}^*(\nu - 1) + \text{c.c.}$$

This overlap of the functions is an expression of the interference in Fourier space, of the contribution from positive- and negative-frequency components. Therefore this coupling of polarization channels to pulse shape is a higher-derivative effect and would depend sensitively on the type of the pulse envelope $g(\varphi)$.

To manifest this effect clearly, we consider finite pulses with the three types of envelope discussed in the Introduction and depicted in Fig. 1. The flat-top pulse has envelope $g(\varphi) = 1$ if $0 < \varphi < \Phi$, and otherwise $g(\varphi) = 0$; the sine-squared pulse has envelope $g(\varphi) = \sin^2[\varphi/(2N)]$ if $0 < \varphi < \Phi$, and otherwise $g(\varphi) = 0$; the Gaussian pulse has envelope $g(\varphi) = \exp[-2.3\varphi^2/(N\pi)^2]$. The pulse phase duration is defined as $\Phi = 2N\pi$.

To measure the relative importance of the photon polarization, we define the quantity

$$R = \frac{|\mathsf{P}_\ell(\Gamma = -1) - \mathsf{P}_\ell(\Gamma = +1)|}{\mathsf{P}_\ell(\Gamma = -1) + \mathsf{P}_\ell(\Gamma = +1)}. \qquad (14)$$

The linear Breit Wheeler positron yield for different probe photon polarizations, and how it is affected by pulse duration, is illustrated in Fig. 8. In general, the yield increases with pulse duration, but it does this slower than linearly with Φ (unlike a local approach, which increases the yield linearly with Φ). This is because the bandwidth decreases and so too, the number of photons from the background that would correspond to a center-of-mass energy above the threshold for making a pair. This behavior depends on the shape of the pulse: slightly different dependencies are shown in Fig. 8(a) (flat-top pulse), Fig. 8(c) (sine-squared pulse) and Fig. 8(e) (Gaussian pulse). The effect of the pulse duration on the ratio of polarized probabilities is shown in the second column of
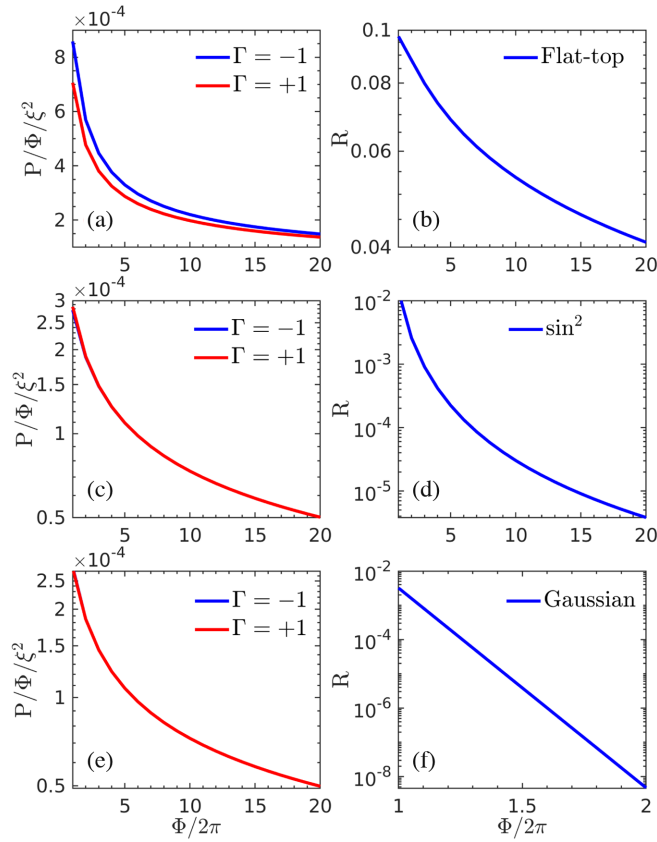

FIG. 8. Left column: total yield, for $\eta = 2$, of the positrons from the linear Breit-Wheeler process normalized by the pulse duration Φ and intensity ξ. Right column: relative importance of the probe photon's polarization in the positron yield R, given in Eq. (14). First row: flat-top pulse, $g(\varphi) = 1$ if $0 < \varphi < \Phi$, and otherwise $g(\varphi) = 0$. Middle row: sine-squared pulse, $g(\varphi) = \sin^2[\varphi/(2N)]$ if $0 < \varphi < \Phi$, and otherwise $g(\varphi) = 0$. Last row: Gaussian pulse, $g(\varphi) = \exp[-2.3\varphi^2/(N\pi)^2]$. The background potential is circularly polarized and the probe photon is linearly polarized. The pulse phase duration is defined as $\Phi = 2N\pi$.

Fig. 8. Similar to the yield, the ratio decreases as the pulse duration is increased, and this is due to reduction of the overlap of positive and negative frequencies of the background in the pulse spectrum. For a flat-top pulse, this decrease is rather slow: for a single-cycle pulse the ratio is 10%, falling to 4% for a 20-cycle pulse. For a sine-squared and Gaussian pulse [Figs. 8(d) and 8(f) respectively], the decrease is much stronger (for the Gaussian pulse, the decrease is rapid, as reflected by the relabeled pulse duration axis), showing the importance of the pulse shape in this effect.

IV. AZIMUTHAL ASYMMETRY

In this section, we calculate a signal of azimuthal asymmetry at the center of the positron TMD, even though the plane-wave pulse is circularly polarized. The asymmetry for different pulse shapes is compared.

The asymmetry induced by the pulse envelope can be illustrated by formulating the relative difference of the transverse spectrum and the azimuthal-averaged spectrum:

$$\mathcal{A} = \frac{d^2\mathsf{P}/drd\psi}{\frac{1}{2\pi}\int_0^{2\pi}[d^2\mathsf{P}/drd\psi]d\psi} - 1.$$

The result for a flat-top background with $\xi = 0.5$, $\eta = 2$ and $N = 16$, in Fig. 9, (using $r_x = r\cos\psi$ and $r_y = r\sin\psi$), amounts to uncovering a dipole-like distribution, which is symptomatic of having linear polarization. This dipole structure is strongest at small transverse momenta r, which corresponds to contributions from the pulse envelope for harmonics below the locally monochromatic threshold. Whereas the carrier frequency is circularly polarized, the pulse envelope multiplies both polarization components of the potential a with the same factor, and hence acts as a "linearly polarized" background. We can demonstrate this by writing the Fourier transform as

$$\tilde{a}(\nu) = m\xi[\tilde{g}(1+\nu)\Lambda_- + \tilde{g}(-1+\nu)\Lambda_+]. \qquad (15)$$

In a monochromatic wave, $\tilde{g}(\cdot) \to \delta(\cdot)$ and the frequency component associated with two different helicity states can never overlap. However, if the pulse is finite in extent, the overlapping between the differently polarized components becomes possible. We pick $\nu = \nu_{\text{pulse}} \approx 1/2N$, to correspond to the pulse envelope frequency, for a symmetric spectrum (such as the flat-top, sine-squared and Gaussian examples), $\tilde{g}(1 + \nu_{\text{pulse}}) \approx \tilde{g}(-1 + \nu_{\text{pulse}})$, and hence

$$\tilde{a}(\nu_{\text{pulse}}) \approx m\xi\tilde{g}(1+\nu_{\text{pulse}})\Lambda_1, \qquad (16)$$

clearly exhibits the property of linear polarization.

The effect persists in pulses with smoother edges as illustrated in Figs. 10(a) and (b) for a sine-squared pulse and in Figs. 10(c) and (d) for a Gaussian pulse. We note that
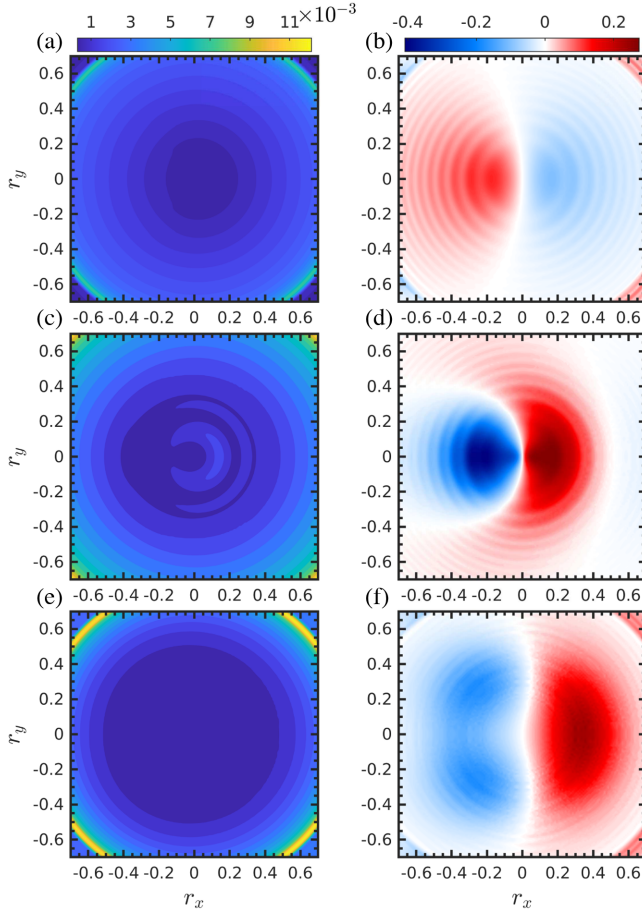
FIG. 9. Azimuthal asymmetry in the transverse momentum distribution of the positron produced in a flat-top pulse for $\eta = 2$, $N = 16$. Left column: plot of the angular spectrum, $d^2\mathsf{P}/dr_x dr_y$. Right column: asymmetry measure, $\mathcal{A}(r_x, r_y)$. Upper panels: $\xi = 0.5$. Middle panels: $\xi = 1.0$. Bottom panels: $\xi = 1.5$.

FIG. 10. Azimuthal asymmetry in the transverse momentum distribution of the positrons. Left column: plot of the angular spectrum, $d^2\mathsf{P}/dr_x dr_y$. Right column: asymmetry measure, $\mathcal{A}(r_x, r_y)$. Upper panels: sine-squared pulse, $g(\varphi) = \sin^2[\varphi/(2N)]$ if $0 < \varphi < 2N\pi$, and otherwise $g(\varphi) = 0$. Bottom panels: Gaussian pulse with the envelope $\exp[-2.3\phi^2/(N\pi)^2]$. The other parameters are given as $\xi = 1$, $\eta = 2$ and $N = 16$.

in these examples, $N = 16$, i.e., this is *not* the short-pulse effect described in Fig. 5. We also note the interference fringes (although not their magnitude) depend sensitively on the shape of pulse envelope; interference peaks appear at different positions for different envelopes, and there appear more interference fringes because of the variation of the local intensity $\xi(\varphi)$. A noteworthy feature of the asymmetry at the center of the positron TMD is that it becomes much weaker when ξ is lowered below $\xi = 1$ for the sine-squared and Gaussian pulses, suggesting an all-order interaction (but persists for $\xi < 1$ in the special case of the flat-top pulse).

V. DISCUSSION

The nonlinear Breit-Wheeler process is often calculated using some local approximation, such as the locally constant field approximation, or the locally monochromatic approximation. The focus of this paper has been to identify
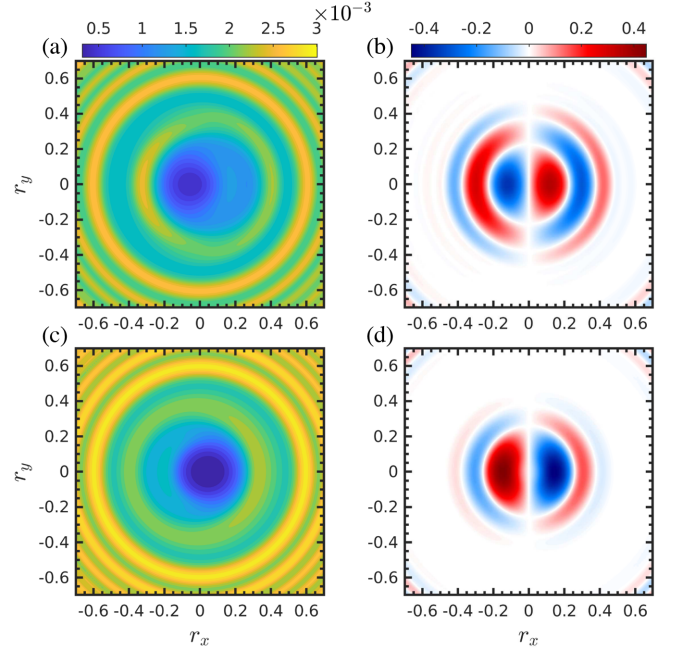
signals of strong-field QED in the nonlinear Breit-Wheeler process, that are beyond local approaches. In order to achieve this, we calculated the process in a toy-model flat-top pulse potential, which differs only from the infinite monochromatic background in that it has edges. The advantage of this background, is that one can make analytical progress and cast the form of the probability for this finite pulse, in a similar form to the probability in an infinite monochromatic wave, and study the differences. Any difference is then due to the finitude of the pulse, and not due to variations of the field strength across the pulse (which, e.g., the locally monochromatic approximation would partially capture). We also calculated some spectra in smoothly varying pulses, with sine-squared and Gaussian envelopes, to investigate how the shape of the pulse envelope influences "beyond local" signatures.

What is missed in a local monochromatic (and locally constant) approach, can be seen by considering the two steps made in approximating the Kibble mass [71], μ, where

$$\mu = 1 + \langle \mathbf{a}^2 \rangle - \langle \mathbf{a} \rangle^2, \qquad \langle f \rangle = \theta^{-1} \int_{\varphi - \theta/2}^{\varphi + \theta/2} f(x) dx.$$

Suppose we consider $\langle \mathbf{a} \rangle$ as an example, and apply the LMA to the function $\mathbf{a}(\varphi) = \mathbf{e}_x g(\varphi/\Phi) \cos \varphi$. First, we can write

$$\langle \mathbf{a} \rangle = \frac{\mathbf{e}_x}{\theta} \left[F\left(\frac{x}{\Phi}\right) \sin x + G\left(\frac{x}{\Phi}\right) \cos x \right]_{\varphi - \theta/2}^{\varphi + \theta/2},$$

where by repeated integration by parts, one finds

$$F\left(\frac{x}{\Phi}\right) = g\left(\frac{x}{\Phi}\right) - \frac{1}{\Phi^2} g''\left(\frac{x}{\Phi}\right) + \cdots,$$

$$G\left(\frac{x}{\Phi}\right) = \frac{1}{\Phi} g'\left(\frac{x}{\Phi}\right) - \frac{1}{\Phi^3} g'''\left(\frac{x}{\Phi}\right) + \cdots$$

For smooth, well-behaved envelopes, so far no approximation has been made. The LMA then consists of two approximations: (i) higher derivatives of g are discarded; (ii) the envelope is locally expanded, keeping only the leading-order term i.e., $g[(\varphi \pm \theta/2)/\Phi] \approx g(\varphi/\Phi)$. The first approximation (also referred to as the slowly-varying-envelope approximation) corresponds to neglecting derivatives of the envelope, and the second to neglecting pulse-envelope interference (which would also include some derivatives of the envelope). Therefore, even if the pulse is long, if the rising and falling edges are steep enough, then signatures beyond a local approximation, can still persist. As a result, we have identified effects on particle spectra due to (i) pulse-envelope interference and (ii) pulse shape effects (contributions from higher derivatives of the rising and falling edge of the pulse).

Other works have already highlighted some interference effects for very short (few cycle) pulses; the added interest here, was to show that there are other pulse-length interference effects that persist even in long (many-cycle) pulses, the magnitude of which does not depend strongly on the pulse shape. One may think that, if the pulse is made long enough, outgoing particle spectra should eventually tend to those in a monochromatic wave. However, the key difference in the finite pulse case, is that the probe particle (in this case, a photon), is, at some point, outside the pulse, and must enter (and exit) it. In the infinite monochromatic case, the probe particle is *always* inside the background. The act of entering (and exiting) the pulse, is associated with the probe particle experiencing field gradients. The

longer the pulse, the lower the gradients, but the longer the scale on which they are probed.

For nonlinear Breit-Wheeler pair creation, pulse envelope interference affected the positron transverse momentum distribution by providing an extra "pulse envelope peak" at smaller transverse momenta than the threshold for a locally monochromatic approach. The position of this pulse envelope peak is associated with the long wavelength of the pulse envelope. The peak was found to lead to a linearly polarized signal in a flat-top, sine-squared and Gaussian pulses, the magnitude of which did not depend significantly on pulse shape. In contrast, effects were also identified that are related to the pulse shape and the contribution from higher derivatives of the envelope. In a flat-top pulse, the relative importance of Breit-Wheeler pair creation for different photon polarizations was seen to be linked to the pulse duration, but was suppressed in the smoother sine-squared and Gaussian backgrounds. The short-pulse asymmetry across the entire positron transverse momentum is another effect sensitive to the pulse shape, and was demonstrated for the flat-top background. A significant widening of the light-front momentum spectrum was also found in a flat-top background, which was independent of the pulse duration.

To conclude: if pulse-shaping methods could be used to generate steeper pulse edges, envelope shape effects could be enhanced, and if low transverse pair momenta could be detected, pulse-length interference effects could be measured in experiment.

ACKNOWLEDGMENTS

[1] G. Breit and J. A. Wheeler, Phys. Rep. **46**, 1087 (1934).

[2] V. I. Ritus, J. Russ. Laser Res. **6**, 497 (1985).

[3] C. N. Harvey, A. Ilderton, and B. King, Phys. Rev. A **91**, 013822 (2015).

[4] A. Di Piazza, M. Tamburini, S. Meuren, and C. H. Keitel, Phys. Rev. A **98**, 012134 (2018).

[5] A. Ilderton, B. King, and D. Seipt, Phys. Rev. A **99**, 042121 (2019).

[6] A. Di Piazza, M. Tamburini, S. Meuren, and C. H. Keitel, Phys. Rev. A **99**, 022125 (2019).

[7] B. King, Phys. Rev. A **101**, 042508 (2020).

[8] D. Seipt and B. King, Phys. Rev. A **102**, 052805 (2020).

[9] H. R. Reiss, J. Math. Phys. (N.Y.) **3**, 59 (1962).

[10] A. I. Nikishov and V. I. Ritus, Sov. Phys. JETP **19**, 529 (1964).

[11] N. B. Narozhnyĭ, Sov. Phys. JETP **28**, 371 (1969).

[12] T. Heinzl, A. Ilderton, and M. Marklund, Phys. Lett. B **692,** 250 (2010).

[13] K. Krajewska and J. Z. Kamiński, Phys. Rev. A **84,** 033416 (2011).

[14] K. Krajewska and J. Z. Kamiński, Phys. Rev. A **86,** 052104 (2012).

[15] A. I. Titov, H. Takabe, B. Kämpfer, and A. Hosaka, Phys. Rev. Lett. **108,** 240406 (2012).

[16] T. Nousch, D. Seipt, B. Kämpfer, and A. Titov, Phys. Lett. B **715,** 246 (2012).

[17] A. M. Fedotov and A. A. Mironov, Phys. Rev. A **88,** 062110 (2013).

[18] A. I. Titov, B. Kämpfer, H. Takabe, and A. Hosaka, Phys. Rev. A **87,** 042106 (2013).

[19] S. Meuren, K. Z. Hatsagortsyan, C. H. Keitel, and A. Di Piazza, Phys. Rev. D **91,** 013009 (2015).

[20] Y.-B. Wu and S.-S. Xue, Phys. Rev. D **90,** 013009 (2014).

[21] M. J. A. Jansen and C. Müller, Phys. Rev. D **93,** 053011 (2016).

[22] S. Meuren, C. H. Keitel, and A. Di Piazza, Phys. Rev. D **93,** 085028 (2016).

[23] T. Nousch, D. Seipt, B. Kämpfer, and A. I. Titov, Phys. Lett. B **755,** 162 (2016).

[24] A. Di Piazza, Phys. Rev. Lett. **117,** 213201 (2016).

[25] M. J. A. Jansen, J. Z. Kamiński, K. Krajewska, and C. Müller, Phys. Rev. D **94,** 013010 (2016).

[26] A. Hartin, A. Ringwald, and N. Tapia, Phys. Rev. D **99,** 036008 (2019).

[27] A. Ilderton, Phys. Rev. D **101,** 016006 (2020).

[28] A. Ilderton, Phys. Rev. D **100,** 125018 (2019).

[29] A. I. Titov, A. Otto, and B. Kämpfer, Eur. Phys. J. D **74,** 39 (2020).

[30] A. I. Titov and B. Kämpfer, Eur. Phys. J. D **74,** 218 (2020).

[31] A. Mercuri-Baron, M. Grech, F. Niel, A. Grassi, M. Lobet, A. D. Piazza, and C. Riconda, New J. Phys. **23,** 085006 (2021).

[32] E. N. Nerush, I. Yu. Kostyukov, A. M. Fedotov, N. B. Narozhny, N. V. Elkina, and H. Ruhl, Phys. Rev. Lett. **106,** 035001 (2011).

[33] N. V. Elkina, A. M. Fedotov, I. Y. Kostyukov, M. V. Legkov, N. B. Narozhny, E. N. Nerush, and H. Ruhl, Phys. Rev. ST Accel. Beams **14,** 054401 (2011).

[34] C. Ridgers, J. Kirk, R. Duclous, T. Blackburn, C. Brady, K. Bennett, T. Arber, and A. Bell, J. Comput. Phys. **260,** 273 (2014).

[35] A. Gonoskov, S. Bastrakov, E. Efimenko, A. Ilderton, M. Marklund, I. Meyerov, A. Muraviev, A. Sergeev, I. Surmin, and E. Wallin, Phys. Rev. E **92,** 023305 (2015).

[36] E. G. Gelfer, A. A. Mironov, A. M. Fedotov, V. F. Bashmakov, E. N. Nerush, I. Y. Kostyukov, and N. B. Narozhny, Phys. Rev. A **92,** 022113 (2015).

[37] T. Grismayer, M. Vranic, J. L. Martins, R. A. Fonseca, and L. O. Silva, Phys. Plasmas **23,** 056706 (2016).

[38] M. Lobet, X. Davoine, E. d'Humières, and L. Gremillet, Phys. Rev. Accel. Beams **20,** 043401 (2017).

[39] F. Wan, R. Shaisultanov, Y.-F. Li, K. Z. Hatsagortsyan, C. H. Keitel, and J.-X. Li, Phys. Lett. B **800,** 135120 (2020).

[40] Y.-Y. Chen, P.-L. He, R. Shaisultanov, K. Z. Hatsagortsyan, and C. H. Keitel, Phys. Rev. Lett. **123,** 174801 (2019).

[41] D. Seipt, C. P. Ridgers, D. Del Sorbo, and A. G. R. Thomas, New J. Phys. **23,** 053025 (2021).

[42] T. Heinzl, B. King, and A. J. MacLeod, Phys. Rev. A **102,** 063110 (2020).

[43] H. Abramowicz et al., Eur. Phys. J. Spec. Top. **230,** 2445 (2021).

[44] T. G. Blackburn, PTARMIGAN (2021), https://github.com/tgblackburn/ptarmigan.

[45] T. G. Blackburn, A. J. MacLeod, and B. King, New J. Phys. **23,** 085008 (2021).

[46] T. G. Blackburn and B. King, arXiv:2108.10883.

[47] C. Bamber et al., Phys. Rev. D **60,** 092004 (1999).

[48] C. Bula et al. (E144 Collaboration), Phys. Rev. Lett. **76,** 3116 (1996).

[49] D. L. Burke et al., Phys. Rev. Lett. **79,** 1626 (1997).

[50] K. Yokoya, User's manual of CAIN version 2.35, KEK Report No. 4/96, 2003.

[51] A. Hartin, Int. J. Mod. Phys. A **33,** 1830011 (2018).

[52] V. Dinu and G. Torgrimsson, Phys. Rev. D **101,** 056017 (2020).

[53] D. Seipt and B. Kämpfer, Phys. Rev. A **88,** 012127 (2013).

[54] K. Krajewska and J. Z. Kaminski, Phys. Rev. A **86,** 052104 (2012).

[55] A. I. Titov, B. Kämpfer, A. Hosaka, T. Nousch, and D. Seipt, Phys. Rev. D **93,** 045010 (2016).

[56] M. J. A. Jansen and C. Müller, Phys. Lett. B **766,** 71 (2017).

[57] A. I. Titov, H. Takabe, and B. Kämpfer, Phys. Rev. D **98,** 036022 (2018).

[58] Z. Peng, H. Hu, and J. Yuan, Phys. Rev. Research **2,** 013020 (2020).

[59] K. Krajewska and J. Z. Kamiński, Phys. Rev. A **90,** 052108 (2014).

[60] R. Schutzhold, H. Gies, and G. Dunne, Phys. Rev. Lett. **101,** 130404 (2008).

[61] C. Kohlfurst, M. Mitter, G. von Winckel, F. Hebenstreit, and R. Alkofer, Phys. Rev. D **88,** 045028 (2013).

[62] H. Gies and G. Torgrimsson, Phys. Rev. Lett. **116,** 090406 (2016).

[63] G. Torgrimsson, C. Schneider, J. Oertel, and R. Schützhold, J. High Energy Phys. 06 (2017) 043.

[64] X.-G. Huang and H. Taya, Phys. Rev. D **100,** 016013 (2019).

[65] T. Heinzl and A. Ilderton, Opt. Commun. **282,** 1879 (2009).

[66] B. King, Phys. Rev. D **103,** 036018 (2021).

[67] S. Tang, Phys. Rev. A **104,** 022209 (2021).

[68] E. Brezin and C. Itzykson, Phys. Rev. D **2,** 1191 (1970).

[69] H. Gies and G. Torgrimsson, Phys. Rev. D **95,** 016001 (2017).

[70] C. Kohlfürst, Phys. Rev. D **99,** 096017 (2019).

[71] L. S. Brown and T. W. B. Kibble, Phys. Rep. **133,** A705 (1964).